Radio Science, Volume 34, Number 4, Pages 949–966, July–August 1999

Analysis and validation of GPS/MET radio occultation data in the ionosphere

William S. Schreiner, Sergey V. Sokolovskiy, Christian Rocken, and Douglas C. Hunt

GPS Science and Technology Program, University Corporation for Atmospheric Research, Boulder, Colorado

Abstract. Global Positioning System (GPS) radio occultation signals received by a low Earth orbit (LEO) satellite provide information about the global distribution of electron density in the ionosphere. We examine two radio occultation inversion algorithms. The first algorithm utilizes the Abel integral transform, which assumes spherical symmetry of the electron density field. We test this algorithm with two approaches: through the computation of bending angles and through the computation of total electron content (TEC) assuming straight line propagation. We demonstrate that for GPS frequencies and for observations in LEO, the assumption of straight-line propagation (neglecting bending) introduces small errors when monitoring the F_2 layer. The second algorithm, which also assumes straight-line propagation, is a three-dimensional (3-D) inversion constrained with the horizontal structure of a priori electron density fields. As a priori fields we use tomographic solutions and the parameterized real-time ionospheric specification model (PRISM) when adjusted with ionosonde data or ground-based GPS vertical TEC maps. For both algorithms we calibrate the occultation data by utilizing observations from the part of the LEO that is closer to the GPS satellite. For inversions we use dual-frequency observational data (the difference of L1 and L2 phase observables) which cancel orbit errors (without applying precise orbit determination) and clock errors (without requiring synchronous ground data) and thus may allow inversions to be computed close to real time in the future. The Abel and 3-D constrained algorithms are validated by statistically comparing 4 days of inversions with critical frequency (f_oF_2) data from a network of 45 ionosonde stations and with vertical TEC data from the global network of GPS ground receivers. Globally, the Abel inversion approach agrees with the f_oF_2 correlative data at the 13% rms level, with a negligible mean difference. All tested 3-D constrained inversion approaches possess a statistically significant mean difference when compared with the ionosonde data. The vertical TEC correlative comparisons for both the Abel and 3-D constrained inversions are significantly biased (~30%) by the electrons above the 735-km LEO altitude.

1. Introduction

Radio occultation is a technique for sounding planetary atmospheres that was pioneered by groups at the Jet Propulsion Laboratory (JPL) and Stanford University over 30 years ago [*Fjeldbo et al.*, 1971]. This technique has been applied to the Earth with the Global Positioning System/Meteorology (GPS/MET) experiment, which uses radio occultation observations of GPS satellites to obtain vertical profiles of refractivity, density, pressure, temperature, and water vapor pressure in the stratosphere and troposphere [*Ware et al.*, 1996; *Kursinski et al.*, 1996; *Rocken et al.*, 1997] and electron density in the ionosphere [*Hardy et al.*, 1993; *Hajj et al.*, 1994; *Leitinger et al.*, 1997; *Hajj and Romans*, 1998].

The GPS/MET instrument orbits the Earth aboard the MicroLab 1 satellite at an altitude of ~735 km with a period of 100 min. Occultations occur as the GPS radio waves propagate through the ionosphere to a receiver in low Earth orbit (LEO), as shown in Figure 1. Twenty-four GPS satellites orbit Earth at ~20,231 km altitude twice a day and broadcast carrier

Paper number 1999RS900034.
0048-6604/99/1999RS900034$11.00

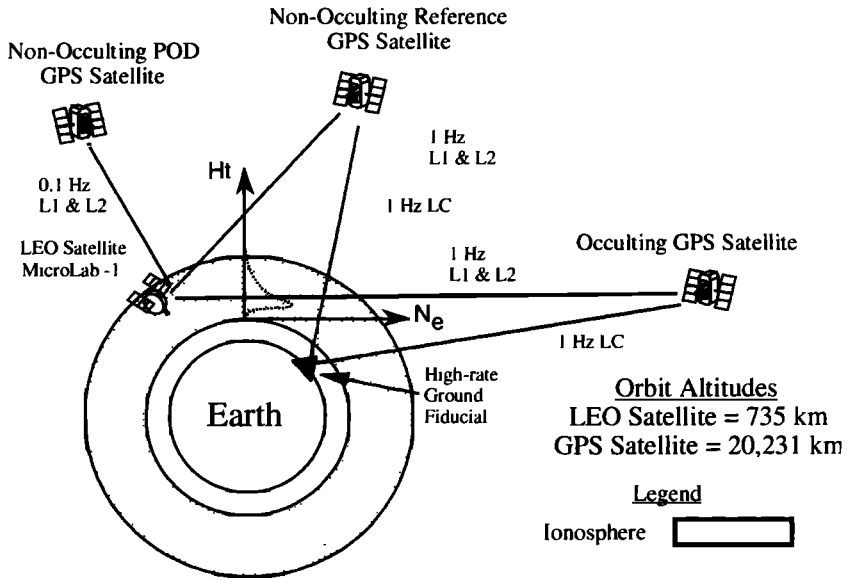

Figure 1. Illustration of the geometry of an occultation in the ionosphere. Also shown are the reference Global Positioning Satellite (GPS) satellite and high-rate GPS ground receiver which are required for single-frequency occultation processing.

signals continuously at 1.57542 GHz (L1) and 1.2276 GHz (L2). Approximately 500 rising and setting occultations may be observed each day from a LEO receiver. The vertical resolution of an ionospheric occultation depends on the receiver sampling interval and the perigee ascent (descent) rate but is fundamentally limited by the Fresnel zone to approximately 1.5 km. However, the occultation geometry provides poor horizontal resolution, and horizontal inhomogeneity of electron density in the region of the occultation is the largest error source for retrieval methods that assume spherical symmetry.

When the GPS/MET instrument tracks a GPS satellite as it is occulted by Earth's ionosphere, it records the carrier phase change on the GPS-to-LEO microwave links (L1 and L2) at 0.1-Hz (nominal rate) and 1-Hz with millimeter-scale precision. After removal of the nominal carrier frequency, the effect of the relative motion between the GPS and LEO satellites, and the effects of clock drifts in the transmitter and receiver, the residual phase on the GPS-LEO link remains, which is related to the speeding up of phase and to the bending of radio waves in the ionosphere. This excess ionospheric delay (as a function of time) on the GPS-to-LEO link is the fundamental observable used by GPS radio occultation inversion techniques to compute electron density profiles. A more detailed discussion of orbit determination and excess phase calibration is provided by *Schreiner et al.* [1998].

The problem of utilizing space radio occultation data is underdetermined, i.e., there is an insufficient number of one-dimensional (1-D) observational data sets to reconstruct a 3-D refractivity field with necessary accuracy and resolution. The general solution of this problem is a 3-D (4-D) tomographic reconstruction with additional observational data. This technique has been developed and tested in a number of papers [see, for example, *Hajj et al.*, 1994; *Leitinger et al.*, 1997; *Rius et al.*, 1997; *Howe et al.*, 1998], but with the lack of ionospheric observational data it is still not robust enough to replace other simpler inversion techniques. These simpler techniques require that additional constraints be imposed on the solution. The most widely used constraint is the assumption of spherical symmetry of refractivity in some region around the tangent points of rays. This assumption provides very good results for neutral atmospheric inversions, where the anisotropy of refractive inhomogeneities, i.e., the ratio of their horizontal to vertical scales, is normally very large. In the ionosphere, anisotropy is much smaller, but still, accord-

ing to *Hajj and Romans* [1998], and according to the results of the present paper, the Abel inversion, which utilizes the spherically symmetric assumption, is the most robust and simple source of information about the vertical structure of electron density. Several attempts have been investigated to weaken the spherically symmetric constraint by using a priori information about the horizontal structure of an electron density field that is either (1) constant in altitude (in an integral form) [*Hardy et al.*, 1993] or (2) a function of altitude [*Hajj et al.*, 1994]. In this paper we follow the technique suggested by *Hajj et al.* [1994] and evaluate it with real GPS/MET data and a priori electron density fields generated with (1) the parameterized real-time ionospheric specification model (PRISM) [*Daniell and Brown*, 1995] when adjusted with global f_oF_2 (critical frequency) data from ionosondes; (2) the PRISM model when adjusted with global ionospheric map (GIM) vertical total electron content (TEC) data; and (3) 3-D tomographic reconstructions of the ionosphere using GPS ground-based and GPS/MET space-based TEC data [*Rius et al.*, 1997]. We statistically validate the results of both the Abel and 3-D constrained inversions with comparisons to correlative observational data (ionosondes and GIM vertical TEC). Using the same data sources for constraints and for validation is reasonable, because constrained inversions use only information about the horizontal structure of a priori electron density fields and not their magnitude. Although validation of the Abel and 3-D constrained inversions is the main goal of this paper, in parallel we discuss in detail some modifications of the inversion techniques which we have applied.

One issue concerns a linearization of the problem. Traditionally, similar to what is done for inversions of neutral atmospheric data, bending angles are calculated from the observational excess phase (Doppler) and are then used to calculate refractivity (electron density) [*Hajj and Romans*, 1998]. However, at GPS frequencies, even under worst-case ionospheric conditions, bending in the ionosphere is small enough so that ray separation from straight-line propagation for observations in LEO is only about several kilometers or less, i.e., much smaller than typical vertical scales of the electron density in the F_2 layer. Since errors resulting from horizontal inhomogeneity are statistically much larger than the change of electron density over the vertical scale of several kilometers, we assume that it is reasonable to neglect bending for monitoring the F_2 layer (this may not be the case for E layer monitoring). Then, under the assumption of straight-line propagation, the excess phase is linearly related to refractivity. Under the additional assumption of spherical symmetry, the Abel inversion can be applied directly to the excess phase observational data. Our comparisons of linear and nonlinear Abel inversions for a large observed F_2 electron density indicate that the difference in the retrieved profiles is negligible in the F_2 layer. Linearization of the inversions allows the use of dual-frequency observational data, i.e., the difference of excess phases for L1 and L2 GPS carriers. This is important, as both orbit and clock errors are automatically canceled, and thus precise orbit determination (POD) and double-differencing with additional ground data are not required, which allows inversions to be performed in near real time.

A second issue considered in the paper is related to the initialization of inversions. Formally, the LEO observational data depend on electron density up to GPS altitudes, but any attempt to solve for the density above the LEO altitudes would weaken the underdetermined problem even more. For inversions of neutral atmospheric data, climatology is normally used above some altitude. For the ionosphere, climatology is not very accurate, so other heuristic methods have been applied, like the extrapolation of the observational data above the LEO altitude [*Hajj and Romans*, 1998]. In the present paper, we apply a technique that allows for a solution of electron density below the LEO only. To do this, we use observational data (excess phase, or calculated bending angles) on both the ascending and descending parts of the LEO with respect to the point of the largest impact distance, and then difference them for a given impact parameter, to calculate their portions below the LEO. This technique implies that the LEO and GPS orbit are close to being coplanar. We assume that the random error introduced by a finite angle between the LEO and GPS orbit may be statistically closer to zero than the errors introduced by using climatology or extrapolation of observational data.

In section 2 we introduce the main equations for refractivity, as well as for bending angle, and excess phase under the assumption of spherical symmetry. Then to substantiate the linearization of the problem, we perform model calculations of these parameters including ray separation from straight-line propagation for a wide range of F_2 peak electron densities. In

section 3 we present the mathematical details of the considered inversion algorithms, which include (1) nonlinear Abel inversion (through bending angles); (2) linear Abel inversion (through TEC); and (3) 3-D inversion (through TEC) constrained with horizontal structure of an a priori electron density field. On the basis of GPS/MET radio occultation data we compare nonlinear and linear Abel inversions (the latter one for single- and dual-frequency data), linear inversions through uncalibrated and calibrated TEC, and inversions using 1-Hz and 0.1-Hz data sampling to test the reconstruction of the F_2 layer. In section 4 we statistically compare the results of Abel and 3-D constrained inversions of GPS/MET data to correlative data. In section 5 we discuss the results and present conclusions.

2. Refractivity and Bending in the Ionosphere

Refractivity in the Earth's ionosphere depends on the density of electrons and ions, the Earth's magnetic field, and carrier frequency. We consider the main term of this dependency, which is proportional to the electron density and inversely proportional to the square of frequency and is defined by

$$n^2 - 1 = -80.6 \times 10^6 N / f^2 \qquad (1)$$

where n^2 is the index of refraction, N is the electron density in el cm^{-3}, and f is the frequency in hertz. Equation (1) is sufficiently accurate for our inversions, because higher-order terms on the right-hand side are several orders of magnitude smaller [*Hardy et al.*, 1993], and the errors that result from neglecting these terms are much smaller than the errors that result from the underdetermination of the inverse problem.

The traditional constraint applied to the underdetermined problem of reconstructing a 3-D refractivity field from 1-D observational data is the assumption of the local spherical symmetry of refractivity in some extended region around the perigees of the sounding rays. Under this assumption the 3-D ray equations may be integrated, resulting in Snell's law. Bending angle α and excess phase S may be explicitly represented in the form of integrals [see, for example, *Phinney and Anderson*, 1968] as follows:

$$\alpha(a) = -a\left[\int_a^{x_{GPS}} + \int_a^{x_{LEO}}\right] \frac{dn/dx}{n(x)\sqrt{x^2 - a^2}}\,dx \qquad (2)$$

$$S(a) = \left[\int_a^{x_{GPS}} + \int_a^{x_{LEO}}\right] \frac{x(1 - xn^{-1}dn/dx)}{\sqrt{x^2 - a^2}}\,dx - L_{GL} \qquad (3)$$

where $a = \rho n(\rho)$ is an impact parameter (ρ is the distance from the ray tangent point to the center of sphericity of the refractivity field), $x = rn(r)$ is a refractional radius (r is radius), and L_{GL} is the distance between the GPS and LEO satellites. Figure 2 illustrates the ray geometry for the case of positive bending (which happens below the F_2 peak), as well as bending angle α and impact parameter a used in (2) and (3).

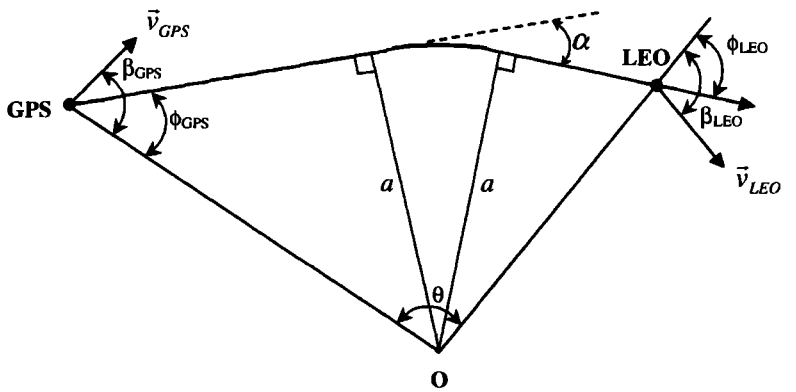

Figure 2. Illustration of the geometry of the ray, bending angle α, and impact parameter a used in the occultation problem. The angles and vectors involved in the relation between Doppler and bending (equation (4)) are also illustrated.

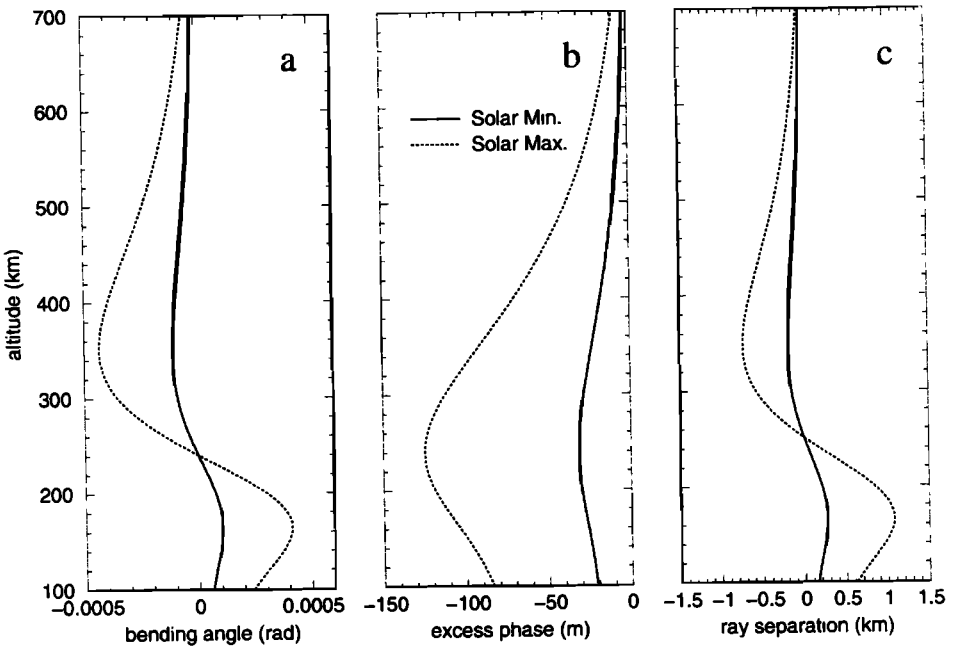

Figure 3. Comparisons of (a) bending angle, (b) excess phase, and (c) L1 ray separation from straight-line propagation (Figure 3c) for typical solar minimum and maximum ionospheric conditions.

In the first term of (2), integration may be expanded to infinity, because ionospheric refractivity is negligible at GPS orbit altitudes. However, this is not the case for LEO (second term). Figure 3 shows example values of bending angle α, excess phase S and an approximate characterization of the maximal ray separation from straight-line propagation ρ - r_0 (r_0 is the impact distance of the straight line connecting the GPS and LEO satellites) versus altitude of the ray tangent point for typical solar minimum and maximum ionospheric conditions. While the bending angle is not strongly dependent on the positions of the GPS and LEO satellites (because both satellites are well above the F_2 peak of the ionosphere), excess phase and ray separation from a straight line connecting the satellites may be very large for satellites far away from Earth.

Calculations for Figure 3 were performed by numerical integration of (2) and (3). We used the L1 frequency (f=f_1). The electron density profile is given by a 1-scale Chapman model with a vertical scale of 75 km, a 300-km F_2 maximum altitude, and electron densities at the F_2 maximum of 5×10^5 and 2×10^6 el cm^{-3}, which model typical daytime ionospheric conditions for the minimum and maximum of the solar cycle [*Flock*, 1987]. In Table 1, bending angles (given impact parameter) and excess phases (given positions of the GPS and LEO satellites) are shown for a wide range of F_2 peak electron densities. The impact parameters and positions were chosen to provide the largest effect below the F_2 peak. Two conclusions can be drawn from Figure 3 and Table 1: (1) Excess phases and bending angles are linear functionals of n – 1 with good accuracy even under worst-case ionospheric conditions, and (2) ray separation from straight-line propagation (for observations from LEO) is small as compared with the vertical scale of the F_2 layer of the ionosphere. We need to note that both conclusions relate to ionospheric structures with vertical scales comparable to the scale

Table 1. Magnitudes of Bending Angle and Excess Phase in the Ionosphere for a Range of Ionospheric Peak Densities

N_{F2}, el cm^{-3}	α, rad	S, m
10^4	2.0602×10^{-6}	-6.2388×10^{-1}
10^5	2.0604×10^{-5}	-6.2389×10^{0}
10^6	2.0615×10^{-4}	-6.2393×10^{1}
10^7	2.0733×10^{-3}	-6.2433×10^{2}

of the F_2 layer, as is our interest in this paper, and may be not be valid for smaller-scale structures like the E layer.

3. Inversion Techniques

3.1. Abel Inversions

In this section we consider Abel inversions of observational data under the assumption of spherical symmetry. First, we examine formulations for the reconstruction of vertical refractivity (electron density) profiles through bending angle data. Next, we look at the reconstruction of refractivity directly from excess phase (TEC) data. Then, we compare the different methods of Abel inversions with each other.

3.1.1. Abel inversion through bending angle data. To calculate bending from excess phase, we use a relation between the Doppler shift of the carrier frequency, $f_d = -fc^{-1}(dS/dt)$, and the projections of the satellite velocities on the ray tangent vectors at the GPS and LEO positions that is given by

$$f_d = f\left[\frac{c - n_{\mathrm{LEO}} v_{\mathrm{LEO}} \cos(\beta_{\mathrm{LEO}} - \phi_{\mathrm{LEO}})}{c - n_{\mathrm{GPS}} v_{\mathrm{GPS}} \cos(\beta_{\mathrm{GPS}} - \phi_{\mathrm{GPS}})} - 1\right] \quad (4)$$

where $\vec{v}_{\mathrm{GPS}}$ and $\vec{v}_{\mathrm{LEO}}$ are 2-D projections of the GPS and LEO satellite 3-D velocities onto the occultation plane (as defined by the GPS satellite, the Earth's center, and the LEO satellite), c is the velocity of light in a vacuum, n_{LEO} and n_{GPS} are the indices of refraction at the LEO and GPS positions, and the angles β and ϕ are illustrated in Figure 2. Equation (4) by itself is insufficient to solve for both ϕ_{GPS} and ϕ_{LEO} given just the Doppler data. Since we assume spherical symmetry of refractivity, we complete (4) with the use of Snell's equation shown below:

$$r_{\mathrm{GPS}} n_{\mathrm{GPS}} \sin\phi_{\mathrm{GPS}} = r_{\mathrm{LEO}} n_{\mathrm{LEO}} \sin\phi_{\mathrm{LEO}} = a \quad (5)$$

By solving (4) and (5) for both ϕ_{GPS} and ϕ_{LEO} with an iterative technique, we obtain both impact parameter a and bending angle α, using

$$\alpha = \phi_{\mathrm{GPS}} + \phi_{\mathrm{LEO}} + \delta - \pi \quad (6)$$

and thus the function $\alpha(a)$. To solve (4) and (5), the refractivities at the GPS and LEO positions are assumed unity, which causes an error of no more than 0.5%, as shown by *Hajj and Romans*, [1998].

The traditional way of solving (2) for a refractivity profile $n(x)$, given a bending angle profile $\alpha(a)$, consists of the formal extension of integration to infinity followed by an application of the Abel transform [*Phinney and Anderson*, 1968]. The solution is given by

$$n(x) = \exp\left[\frac{1}{\pi}\int_x^\infty \frac{\alpha(a)}{\sqrt{a^2 - x^2}} da\right] \quad (7)$$

This solution formally requires knowledge of the full bending angle up to infinitively large values of the impact parameter, which cannot be determined from the GPS-LEO observations. In practice, some heuristic approaches are applied; the bending angles above the LEO are either neglected, replaced by some climate model, or somehow extrapolated [*Hajj and Romans*, 1998]. For extrapolations, it should be noted that the bending angle at the top of the profile should be doubled, because (as seen from Figure 4) the observed bending angle at the LEO altitude constitutes only approximately one half of the full bending (the GPS satellite may be considered outside of the ionosphere).

To avoid observing or extrapolating the bending angle above the LEO, an alternative statement of the inverse problem given by (2) can be used to solve for the refractivity (electron density) below the LEO only. In this statement the observational data are not the bending angle between the GPS and LEO satellites, $\alpha(a) = \alpha_{AC}(a)$, but the bending angle between LEO and another point of the ray having the same altitude as the LEO satellite, $\tilde{\alpha}(a) = \alpha_{BC}(a)$, as shown in Figure 4. We call $\tilde{\alpha}(a)$ a "calibrated" bending angle. In this statement of the problem, (2) takes the form

$$\tilde{\alpha}(a) = -2a\int_a^{x_{LEO}} \frac{dn/dx}{n(x)\sqrt{x^2 - a^2}} dx \quad (8)$$

and its solution is given by

$$n(x) = n(x_{\mathrm{LEO}}) \exp\left[\frac{1}{\pi}\int_x^{x_{LEO}} \frac{\tilde{\alpha}(a)}{\sqrt{a^2 - x^2}} da\right] \quad (9)$$

Solving the inverse problem above based on GPS-LEO observational data requires some additional approximations, which include the GPS satellite be in

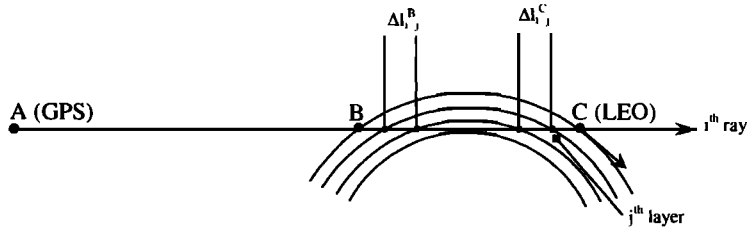

Figure 4. Illustration of the geometry of the total electron content (TEC) and bending angle calibration technique. The discrete representation of the direct operator for the constrained inversion (equation (16)) is also illustrated.

(or close to) the LEO plane and the LEO be close to circular. To compute calibrated bending angles, we at first calculate the bending angle as a function of impact parameter (from Doppler observational data, based on equations (4-6)) for both sides of the orbit with respect to the point with the maximal impact parameter (see Figure 4), i.e., $\alpha_{AC}(a)$ and $\alpha_{AB}(a)$. Then we calculate their difference given impact parameter, $\alpha_{BC}(a) = \alpha_{AC}(a) - \alpha_{AB}(a)$, which represents the bending angle along the section of a ray below the LEO, i.e., $\tilde{\alpha}(a)$. If the GPS satellite is not in the LEO plane, then some error will be introduced due to horizontal inhomogeneity of electron density in the ionosphere. It is natural, however, to assume that this error will be statistically closer to zero than the errors for the case when using the traditional inversion technique for GPS-LEO bending angles, $\alpha(a) = \alpha_{AC}(a)$, and applying heuristic methods for the missing data above the LEO.

As seen from (9), the solution formally depends on refractivity at the LEO position $n_{\mathrm{LEO}} = n(x_{\mathrm{LEO}})$. Setting this refractivity at the LEO to 1 when reconstructing the refractivity profile introduces extra error in addition to the error introduced in the calculation of bending angle from Doppler (discussed before). However, these errors cancel in the first order of magnitude in $n_{\mathrm{LEO}} - 1$ (see Appendix A). Thus the residual error after the inversion of calibrated bending angles is of second order of magnitude in $n_{\mathrm{LEO}} - 1$ and is therefore smaller than the residual error estimated by *Hajj and Romans* [1998] for inversions of the uncalibrated GPS-LEO bending angles.

3.1.2. Abel inversion through total electron content data. Total electron content (TEC) T along a ray is related to electron density N, index of refraction n, and excess phase S by

$$T = \int N dl = -\frac{f^2}{40.3\times 10^6}\int (n-1)dl = -\frac{f^2 S}{40.3} \quad (10)$$

where S is in meters and T is in el m^{-2}. TEC may be calculated from excess phase at either the L1 or L2 GPS carrier frequencies, i.e., from S_1 or S_2. Since formally the L1 and L2 signals propagate on different paths, the calculated TECs will be slightly different. However, as seen in Figure 3, bending and ray separation at GPS frequencies (and for observations in LEO) may be negligible for monitoring the F_2 layer. When bending is neglected (i.e., in the assumption of straight-line propagation) the TEC is the same whether calculated from either S_1 or S_2, or from $S_1 - S_2$, as shown below:

$$T = -\frac{S_1 f_1^2}{40.3} = -\frac{S_2 f_2^2}{40.3} = \frac{(S_1 - S_2) f_1^2 f_2^2}{40.3(f_1^2 - f_2^2)} \quad (11)$$

When calculating TEC from S_1 or S_2 single-frequency data, it is necessary to precisely remove the effects of both orbital motion (via precision orbit determination) and the drifts of the GPS transmitter and receiver clocks (via double-differencing or similar) from the phase data, both of which require GPS ground data and additional data processing. An estimate of the impact that orbit errors have on single-frequency inversions is given in Appendix B. An inherent advantage of using $(S_1 - S_2)$ to calculate TEC is that both the orbit and clock errors are automatically eliminated in the difference. This benefit greatly reduces the required amount of data processing and will allow electron density profiles to be computed on orbit and disseminated in near real time for future missions. The disadvantage of using $(S_1 - S_2)$ is that the additional L2 noise introduced into the TEC data may degrade the inversion results, especially when antispoofing (A/S) is activated. However, the L2 noise is not expected to be an important error source for future missions with improved L2 tracking loops and higher gain antennas.

As in the case of the inversions through bending angles, we use the assumption of spherical symmetry of electron density for TEC inversions. Then the TEC, defined in (10), is related to electron density through the following integral:

$$T(r_0)=\left[\int_{r_0}^{r_{GPS}}+\int_{r_0}^{r_{LEO}}\right]\frac{rN(r)}{\sqrt{r^2-r_0^2}}dr \tag{12}$$

As is similarly done with inversions through bending angles, we calibrate the TEC data along the section of a ray below the LEO, $\tilde{T}(r_0)=T_{BC}(r_0)=T_{AC}(r_0)-T_{AB}(r_0)$, as illustrated in Figure 4. To do this, we at first calculate the straight-line impact distances, r_0, for all observational data on both sides of the LEO with respect to the point with the maximal impact distance. Next, using cubic splines, we interpolate the uncalibrated TEC as a function of impact distance onto some uniform grid. Then, we perform the calibration of TEC, i.e., the calculation of $\tilde{T}(r_0)$ on the given uniform grid r_0. For calibrated TEC, equation (12) transforms into

$$\tilde{T}(r_0)=2\int_{r_0}^{r_{LEO}}\frac{rN(r)}{\sqrt{r^2-r_0^2}}dr \tag{13}$$

The solution of (13) is given by

$$N(r)=-\frac{1}{\pi}\int_{r}^{r_{LEO}}\frac{d\tilde{T}/dr_0}{\sqrt{r_0^2-r^2}}dr_0 \tag{14}$$

As seen from (14), the initial condition (i.e., refractivity or electron density at the LEO altitude) is not required for inversions through calibrated TEC (see also Appendix A).

3.1.3. Comparisons of different methods of Abel inversions. In this section we perform case study comparisons of different methods of Abel inversion which include (1) comparisons of bending angle and TEC inversions using single- and dual-frequency data; (2) comparisons of inversions using calibrated and uncalibrated TEC data; and (3) comparisons of inversions using 1-Hz and 0.1-Hz sampled data.

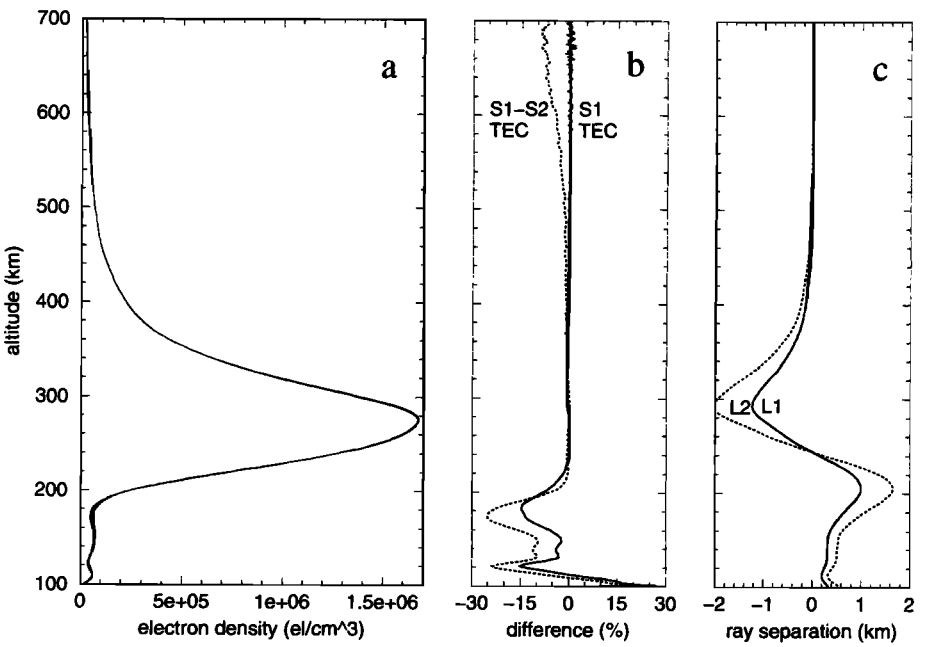

Figure 5. Comparisons of bending angle and TEC inversions with single- and dual-frequency data. Figure 5a shows electron density profiles reconstructed with L1 bending angles (profile 1); S_1 TEC (profile 2); and $S_1 - S_2$ TEC (profile 3). Figure 5b shows the percent differences between profiles 2 and 3 and profile 1. Figure 5c shows the corresponding L1 and L2 ray separation from straight-line propagation.

First, we compare inversions calculated from L1 bending angles and from S_1 and $S_1 - S_2$ TECs (by neglecting bending). These comparisons illustrate good agreement between the inversion methods listed above. For this purpose we use an occultation (University Corporation for Atmospheric Research (UCAR) ID 0398) that took place on February 20, 1997 (1338 UTC, 19.9° latitude, and −19.2° longitude), which is characterized by a very large electron density (~1.7×10^6 el cm^{-3}) within a GPS/MET observational prime time (A/S off).

Figure 5a shows electron density profiles reconstructed from 1-Hz observational data through bending angles calculated from L1 (profile 1); TEC calculated from S_1 (profile 2); and TEC calculated from $S_1 - S_2$ (profile 3). Profiles 1-3 are obtained without calibration of bending angles or TEC as discussed above, because the goal of this comparison is to understand the impact of nonlinearity on inversions. In addition, initialization of the inversions (i.e., extrapolation of observational bending or TEC above the LEO altitude) is not applied. Since it is difficult to distinguish the three profiles given in Figure 5a, the fractional differences relative to the L1 bending angle inversion are shown in Figure 5b. Figure 5c introduces L1 and L2 ray separation from the straight-line propagation path between the GPS and LEO satellites. It can be seen that the fractional differences between the electron densities retrieved by different inversions are less than 1% around the F_2 peak, which are much smaller than errors resulting from horizontal inhomogeneity of the electron density field. The largest fractional difference is about 20-25% in the region of the E layer, which is also the region of the biggest fractional errors resulting from horizontal inhomogeneity of electron density. It should be noted that the differences shown in Figure 5 also contain orbit errors, which mostly affect the solutions using single-frequency data. Also noticeable is the fractional difference between $S_1 - S_2$ TEC and both S_1 TEC and L1 bending solutions at the top of the profile. Since the vertical gradient of electron

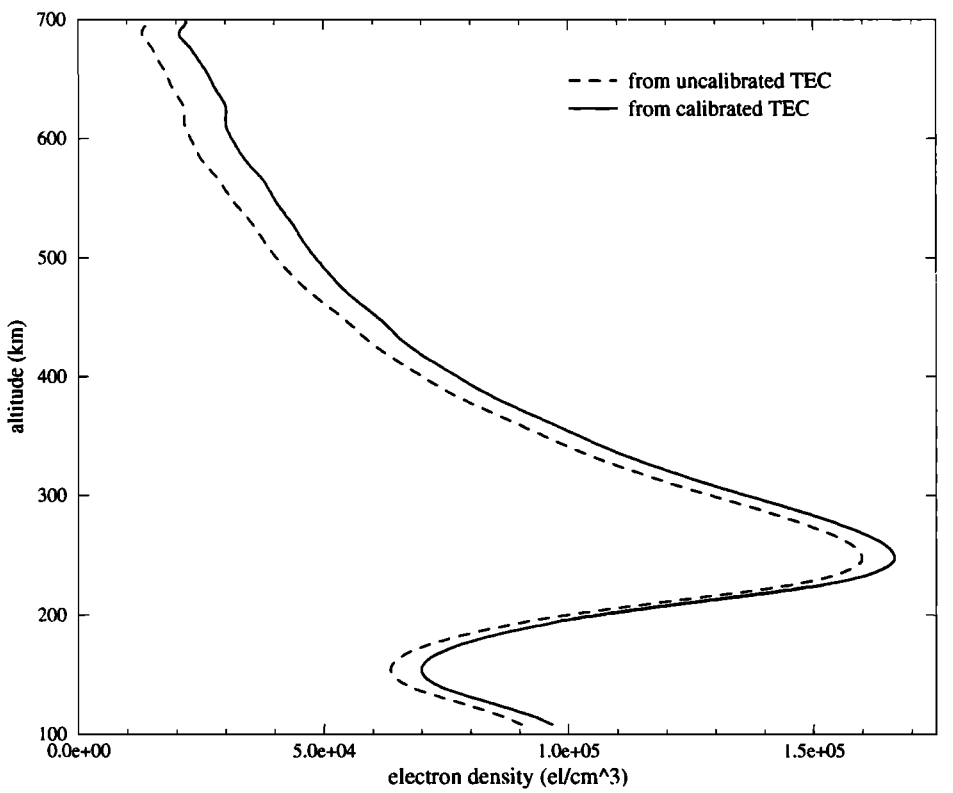

Figure 6. Abel inversions using calibrated and uncalibrated TEC. This comparison shows that for some occultations the calibration of observational data results in noticeable electron density differences at all altitudes.

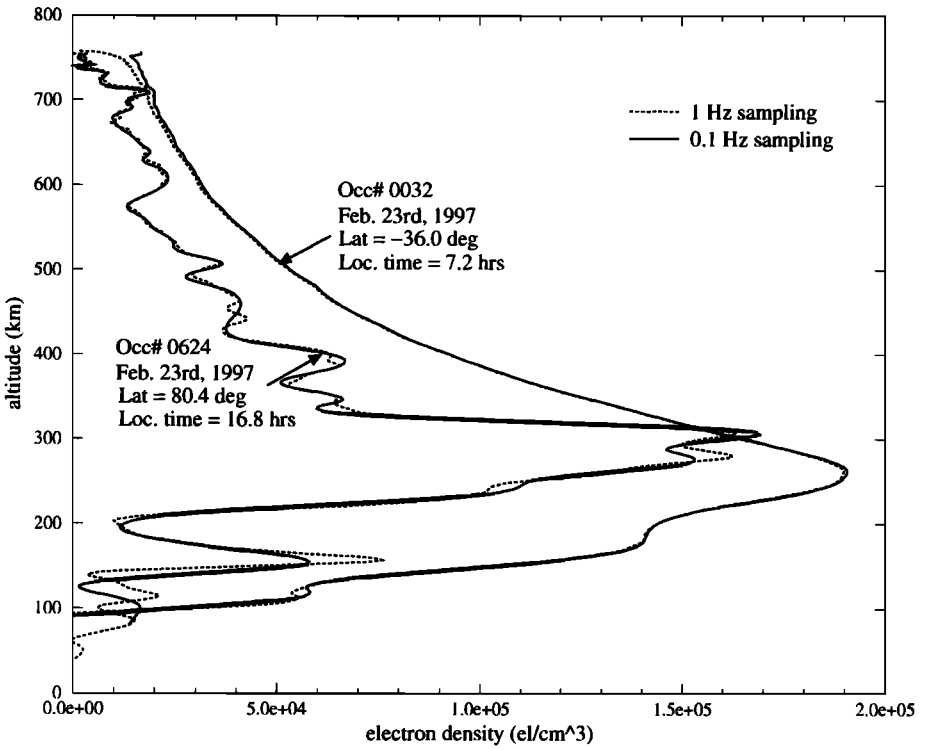

Figure 7. Inversions for two occultations using 0.1- and 1-Hz data. The 0.1-Hz and 1-Hz sampled data are adequate for monitoring the large-scale features of the ionosphere such as F_2 layer (but may not be sufficient for monitoring smaller-scale features such as the E layer).

density and the related nonlinearity are small at those altitudes, and there is no noticeable differences between S_1 TEC and L1 bending angle solutions, it is natural to assume that the difference is caused by residual orbit errors (remaining after POD).

Next we compare an inversion that is calculated with uncalibrated and calibrated TEC. We use an occultation (UCAR ID 0001) which took place on February 23, 1997 (0001 UTC, 66° latitude, and -135° longitude).

Figure 6 shows plots of electron density profiles that are reconstructed from calibrated and uncalibrated TEC obtained from $S_1 - S_2$. The purpose of this comparison is to show that for some occultations the calibration of observational data results in noticeable electron density differences at all altitudes. This is in contrast to the extrapolation technique, which normally results in differences only near the top of the profile.

To examine the effect that the sampling rate has on the reconstruction of the F_2 layer , we compare the results of inversions using 1-Hz and 0.1-Hz data. For this purpose we take inversions using uncalibrated TEC obtained from $S_1 - S_2$. For the 1-Hz inversions we filter (smooth) the excess phase data with a sliding cubic polynomial regression with a 10-s window. For the 0.1-Hz inversions, we apply a cubic spline interpolation of the excess phase data instead of filtering. For comparison we examine two occultations (UCAR IDs 0032 and 0624) that occurred on February 23, 1997. The reconstructed electron density profiles are shown in Figure 7. Occultation 0032 occurred at 36.0° south latitude and at 0712 LT. The electron density profile is comparatively smooth and resolved similarly by both the 1- and 0.1-Hz inversions. Occultation 0624 occurred at 80.4° north latitude at 1648 LT. This reconstruction displays many fluctuations of electron density that are slightly better

resolved by the 1-Hz inversion. However, it appears that both 1-Hz and 0.1-Hz data have sufficient resolution to resolve the F_2 layer, while both sampling rates may be insufficient for monitoring of the E layer.

3.2. Three-Dimensional Constrained Inversions

The Abel inversion is the simplest constrained inversion, as it limits the space of solutions to spherically symmetric functions. Generally, limiting the space of solutions results in solving a least squares problem with respect to the observational data. Here we will follow the method originally proposed by *Hajj et al.* [1994]. In this method, a solved-for 3-D electron density function is represented in the form of a product of some given (model) 3-D function and an unknown vertical scaling function. This scaling function is estimated through a least squares fit to observational TEC data. This solution (as a function of spherical coordinates) has the same latitudinal and longitudinal structure as the model function for each spherical layer, while a scaling factor for each layer is estimated. Thus, although the solution is a 3-D field, the actual dimension of the inverse problem is reduced to 1. The inverse problem is stated as follows:

$$\int_{r_0^{\min}}^{r_0^{\max}} \left| \int_0^{L(r_0)} N^*(\vec{r}(r_0))c(r)dl(r_0) - T_{\text{obs}}(r_0) \right|^2 dr_0 = \min \qquad (15)$$

where $T_{\text{obs}}(r_0)$ is the observational TEC along the ray connecting the GPS and LEO satellites given an impact distance r_0, $\vec{r}(r_0)$ is the position of a point on that ray, $dl(r_0)$ is the differential of length along that ray, and $L(r_0)$ is the total length of that ray. $N^*(\vec{r})$ is a 3-D model electron density field, and $c(r)$ is the solved-for vertical scaling profile. Since we solve for electron densities below the LEO, we use TEC calibrated within the LEO (as discussed in previous sections). In discrete representation, when $i = 1,\ldots,$ is a number of the ray and $j = 1,\ldots,$ is a number of the ionospheric spherical layer, equation (15) transforms into (repeating indices imply summation, and superscripts B and C denote different sides with respect to ray tangent point)

$$\left|(N_{ij}^{*B}\Delta l_{ij}^B + N_{ij}^{*C}\Delta l_{ij}^C)c_j - T_i\right|^2 = \left|A_{ij}c_j - T_i\right|^2 = \min \qquad (16)$$

where the operator (matrix) A_{ij} provides TEC (for the model field) along those sections of the ith ray which are inside the jth ionospheric layer, as illustrated in Figure 4. The solution to (16) (in the operator form) is

$$\vec{c} = (\hat{A}^T\hat{A})^{-1}\hat{A}^T\vec{T} \qquad (17)$$

where superscript T denotes the transpose operator.

Here we briefly list some properties of the discussed constrained inversion. It follows from the statement of the problem given by (15) that multiplication of $N^*(\vec{r})$ by an arbitrary spherically symmetric function $\xi(r)$ does not affect the solution. If a spherically symmetric function $N^*(r)$ is applied as a constraint, then the solution is identical to the Abel inversion regardless of $N^*(r)$. Internal tests show that the differences between the Abel inversion and the constrained inversion with a spherically symmetric model function are negligible and can be attributed to different numerical algorithms. As seen from (17), the solution c is linear with respect to the observational data T but is nonlinear with respect to A (i.e., with respect to the model electron density field N^*). This nonlinearity indicates that the results of the constrained inversion may be biased statistically.

Constrained inversions using (17) sometimes result in negative electron densities at some altitudes. This may be caused by large differences in spatial structures between the true and a priori electron density fields. This also applies to the Abel inversion. To restrict negative solutions, we state the following problem instead of (16):

$$\left|A_{ij}c_j^2 - T_i\right|^2 = \min \qquad (18)$$

However, equation (18) is nonlinear with respect to c and thus cannot be solved explicitly. To solve (18), we apply an iterative gradient method that requires significant processing time. To minimize the processing time for each inversion, we first process the linear solution (equation (17)) that is quite fast. If it provides negative electron densities, we then solve the nonlinear problem (equation (18)). Internal tests show that for those occultations that provide positive electron densities at all altitudes, the differences between the linear and nonlinear solutions are negligible.

The a priori electron density fields used in this paper to constrain the 3-D inversions are obtained from

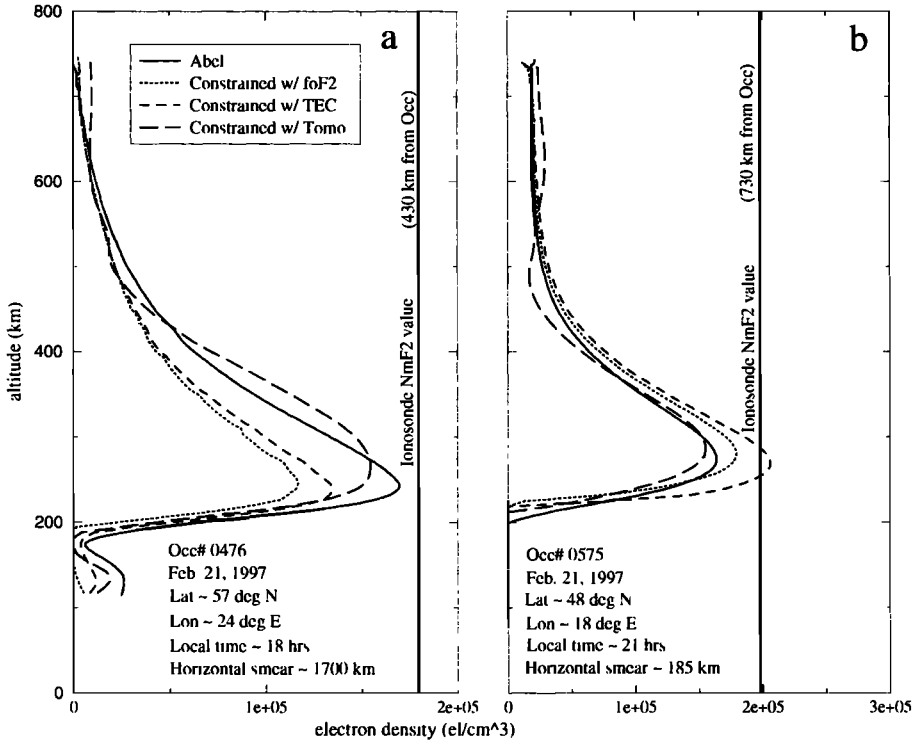

Figure 8. Comparisons of Abel and constrained inversions for two occultations in the postsunset ionosphere. The Abel inversion compares with the ionosonde f_0F_2 data better than the constrained inversions for the occultation in Figure 8a. Figure 8b shows an occultation where the inversion constrained with the parameterized real-time ionospheric specification model (when adjusted with GPS vertical TEC) performs the best.

(1) adjustments of the PRISM model with ionosonde f_0F_2 data; (2) adjustments of the PRISM model with GPS-derived vertical TEC data; and (3) 3-D tomographic reconstructions of the ionospheric electron density from ground-based GPS data and space-based GPS/MET data. PRISM is first initialized to climatology with the date and time of the occultation, $F_{10.7}$ (10.7-cm radio flux) and *Kp* (Earth geomagnetic activity indicator). It is then adjusted with ionospheric data to improve its specification. The ionosonde f_0F_2 data used to adjust PRISM are recorded hourly from a network of 45 global sites and are available from the National Geophysical Data Center (NGDC) in Boulder, Colorado. The GPS vertical TEC data are provided by JPL in the form of hourly GIMs of vertical TEC with a resolution of 2° by 2° in geodetic latitude and longitude [*Mannucci et al.*, 1998].

Three-dimensional electron density fields extracted from 4-D tomograhic solutions based on ground GPS data and GPS/MET data [*Rius et al.*, 1997] are also used to horizontally constrain the inversions. To provide the highest resolution possible and to minimize temporal variability, the tomographic reconstructions are generated in a band +/-20° about the GPS/MET orbit plane in a Sun-fixed reference frame. In particular, the solutions are generated with a resolution of 3 hours in time, 120 km in altitude, 10° in the latitude direction, and 12° in the longitude direction.

Figure 8 compares the three different constrained inversion solutions with Abel solutions and correlative ionosonde N_mF_2 data for two different occultations. Figure 8a shows an example occultation where the Abel inversion performs better than any of the constrained inversion approaches. Figure 8b shows a

comparison where the Abel solution does not perform as well as the constrained solutions that use PRISM with f_oF_2 and TEC data. Both occultations in Figure 8 occur near the postsunset ionosphere, where horizontal gradients can be expected.

4. Statistical Comparisons With Correlative Data

In this section we statistically compare the Abel and 3-D constrained GPS/MET inversions to ionospheric correlative data. For our comparisons we have processed GPS/MET occultations from 4 days (February 20-23) in 1997 when A/S was off. The equatorial crossing times of the GPS/MET orbit during this period are approximately 0900 and 2100 LT, providing mostly morning and evening occultations. The average values for the $F_{10.7}$ radio flux and daily Kp (the sum of the eight 3-hour Kp) for the 4-day period were 71.9 W m^{-2} Hz^{-1} and 14.6, respectively, which indicate fairly quiet ionospheric conditions. The GPS/MET inversions used for the statistical comparisons in this paper are computed using 0.1-Hz dual-frequency TEC ($S_1 - S_2$) data, calibrated with data from the opposite side of the occultation (as discussed in previous sections). No effort is made to cull the statistics to use only the occultations that are close to the GPS/MET orbit plane. The statistics in this paper are subjected to a 3σ outlier test to remove erroneous samples.

4.1. Correlative Data

The Abel and 3-D constrained GPS/MET inversions are compared with ionosonde data (f_oF_2 in MHz and N_mF_2 in el cm^{-3}) and to GIM maps of vertical TEC (in TECU; 1 TECU = 10^{16} el m^{-2}). These correlative data sources are somewhat complementary in that the f_oF_2 measurement is a point measurement in the profile and the vertical TEC measurement is an integral measure of the profile. It is appropriate to use the f_oF_2 and vertical TEC data as both an a priori constraint to the inversions and as comparison data, because the constrained inversions use only the horizontal structure information of the field and not its absolute magnitude.

4.2. Abel Inversion Comparisons

The Abel inversion provides a vertical electron density profile (N versus altitude) assuming spherical symmetry. In practice, we assign this profile to the latitude and longitude of the tangent point of the ray at the altitude of the reconstructed F_2 peak.

To compare the Abel inversions with ionosonde data, we calculate critical frequency of the F_2 peak (i.e., the minimal frequency that allows vertical propagation through the whole ionosphere) with the following equation:

$$f_oF_2 = 8.98 \times 10^{-3} \sqrt{N_mF_2} \tag{19}$$

where N_mF_2 is the electron density of the F_2 peak in el cm^{-3} and f_oF_2 is the critical frequency of the F_2 peak in MHz. We compare GPS/MET-derived f_oF_2 data with the closest ionosonde f_oF_2 data within 1200 km of the reconstructed GPS/MET profile. The hourly ionosonde data are interpolated to the occultation time of interest.

To compare the Abel inversions to GIM vertical TEC data, the electron density profile is integrated from orbit altitude to the ground to obtain an equivalent measurement of subsatellite vertical TEC. We compare the GPS/MET vertical TEC to GIM data that are interpolated to the assigned position and time of the reconstructed profiles.

Figure 9 and Figure 10 show the results of comparisons of the GPS/MET Abel inversions with the

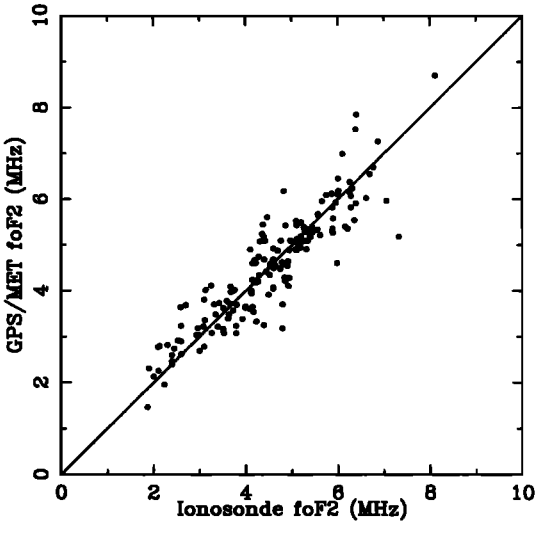

Figure 9. Plot of GPS/MET Abel inversions versus ionosonde (f_oF_2) data from February 20 to 23, 1997. The mean and rms deviation for 163 matches are –0.002 MHz and 0.53 MHz, respectively.

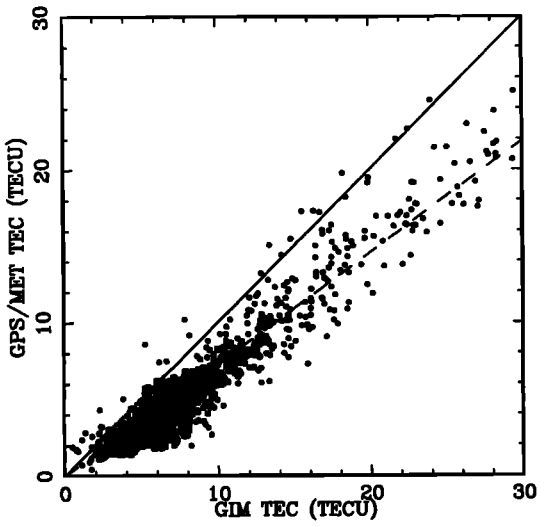

Figure 10. Plot of GPS/MET Abel inversions versus Jet Propulsion Laboratory global ionospheric map (vertical TEC) data. The dashed line shows a linear regression (constrained through zero). The mean and rms deviation for the 783 matches are –2.8 and 1.9 TECU, respectively. The linear regression rms deviation is 1.55 TECU.

ionosonde f_oF_2 data and the GIM vertical TEC data, respectively. The total number of occultations compared with ionosondes within the chosen period is 163, and the total number of occultations compared with GIM TEC data is 783. There are more GIM TEC comparisons than f_oF_2 comparisons, because the GIM data exist for all occultations and the ionosonde data exist for only those occultations with a matching ionosonde. The ionosonde comparison in Figure 9 shows good agreement, with a minimal mean difference. However, the GIM TEC comparisons exhibit a significant bias. The mean and standard deviations of the fractional differences (in percent) between the Abel inversions and the ionosonde critical frequency and GIM TEC data are summarized in the first two rows of Table 2. As seen from Table 2, reconstructed values of f_oF_2 agree at the 13% rms level (26% rms in N_mF_2), with a marginally significant mean difference. This agreement improves slightly when the comparison is performed over the continental United States (CONUS) and Europe. Also as evident in Table 2, the reconstructed GPS/MET vertical TEC data are significantly biased low with respect to the GIM TEC at about the 30% level. This is explained by that portion of the ionosphere above the LEO altitude, which is not reconstructed from the radio occultation data.

4.3. Three-Dimensional Constrained Inversion Comparisons

Constrained inversions formally provide us with a 3-D electron density field. Thus, for comparisons with ionosondes we calculate the vertical electron density profile (and the corresponding f_oF_2/N_mF_2 information) at the site of the ionosonde. We compare GPS/MET-derived f_oF_2 data with the ionosonde f_oF_2 data that are within 1200 km of the assigned position of the profile after the Abel inversion. Again, the hourly ionosonde data are interpolated to the occultation time of interest. To compare the constrained inversions to GIM vertical TEC data, the electron density profile is integrated as is done for the Abel statistics. We compare the GPS/MET vertical TEC to the GIM data at the assigned position and time of the profiles reconstructed by the Abel inversion.

The a priori electron density fields used to constrain the 3-D inversions are obtained from (1) adjustments of the PRISM model with ionospheric data and (2) 3-D tomographic reconstructions of ionospheric electron density. When applying these electron density fields as constraints for our inversions, we process only those occultations that take place over CONUS and Europe. We do this because we are sure there are enough observational data in these regions to improve the horizontal structure of the PRISM electron density fields and to make the tomographic solutions more robust.

The results of the f_oF_2/N_mF_2 and TEC comparisons for the PRISM and tomographic constrained inversions are summarized in Table 2. Since the number of constrained inversions is not high, our results must be considered preliminary. Generally, the constrained inversions show a statistically significant negative bias when compared with the ionosonde data. This might be explained by the nonlinearity of the constrained solutions with respect to the a priori electron density fields, discussed earlier.

5. Discussion and Conclusions

This paper summarizes the research effort performed to develop and validate GPS radio occultation retrieval algorithms for obtaining large-scale profile information in the Earth's ionosphere. The two algorithms that are discussed in detail include the tradi-

Table 2. Summary of Statistical Comparisons of the Abel and Three-Dimensional Constrained Inversions to Correlative Data

	Comparisons to Ionosondes f_0F_2 and N_mF_2			Comparisons to GIM TEC		
	Number of Matches	Mean f_0F_2 % N_mF_2 %	RMS f_0F_2 % N_mF_2 %	Number of Matches	Mean %	RMS %
Abel inversion	164	1.3	12.9	787	-32.2	16.9
(world)	163	2.6	26.0			
Abel inversion	35	-1.4	9.6	39	-24.0	36.3
(Continental United States and Europe)	35	-1.9	18.9			
PRISM	33	-7.1	11.1	31	-29.6	38.6
constrained inversion by ionosondes	33	-12.6	20.5			
PRISM	35	-4.4	11.8	33	-33.3	20.9
constrained inversion by TEC	35	-7.2	22.1			
Tomography	17	-5.9	14.5	16	-30.1	36.0
constrained inversions	17	-9.3	25.2			

tional Abel inversion and the 3-D inversion that is constrained with the horizontal structure of an a priori 3-D electron density field. The GPS/MET inversions used for statistical comparisons in this paper are computed with 0.1-Hz dual-frequency TEC ($S_1 - S_2$) data. The errors incurred by not processing single-frequency bending angle data are shown to be minimal when the interest is large-scale features in the ionosphere. The GPS/MET inversions are also calibrated with TEC data from the side of the LEO closer to the GPS satellite. This calibration technique results in solving for electron density below the LEO only and does not require initialization of inversions. We believe this calibration technique introduces errors that are statistically closer to zero than the errors introduced by initializing the inversions with climatology or the extrapolation of observational data.

The Abel and 3-D constrained algorithms are validated by statistically comparing 4 days (February 20-23, 1997, A/S off) of GPS/MET inversions with f_0F_2 data from a network of 45 ionosonde stations and with vertical TEC data from the global network of GPS ground receivers. Globally, the Abel inversion approach agrees with the f_0F_2 correlative data at the 13% (~0.5 MHz) rms level, with a negligible mean difference. Over CONUS and Europe, the results improve slightly to approximately the 10% rms level. These results are comparable to those published by *Hajj and Romans* [1998]. The accuracy of the ionosonde f_0F_2 data is approximately 0.1 MHz (H. Kroehl, personal communication, 1998), considerably less than 0.5-MHz level. Possible sources of difference that may be contributing significantly to the 13% rms include a breakdown of the spherical symmetry assumption in the region of the occultation plane near high-gradient regions, additional error due to the assumption of spherical symmetry for occultations that are off to the side of the LEO (~3000 km of smear for 45° azimuth angle), the error introduced by calibrating the TEC data, the inherent spatial variability of the ionosphere along with the fact that a correlative matching criterion of 1200 km (the average match distance is 680 km) is used in this study, and the temporal variability which is not captured by the hourly ionosonde data and which also affects the inversion results due to the finite time of each occultation.

The addition of horizontal information (PRISM

adjusted with ionosonde data; PRISM adjusted with vertical TEC data; and 3-D tomographic reconstructions) to the 3-D constrained inversions does not appear to improve upon the Abel inversion statistics. When compared with the f_oF_2 data, the 3-D constrained inversion approaches appear to perform only slightly worse than the Abel approach in terms of the percent rms, but they all possess statistically significant mean differences (5-7%). These mean differences appear to be caused by a nonlinearity of the constrained solutions with respect to the a priori electron density fields.

The GIM vertical TEC correlative comparisons for both the Abel and constrained inversions generally agree at near the 30% rms level, with significant mean differences of approximately 30% (~3 TECU). Our observed large mean differences are apparently due to the fact that the GPS/MET-derived TEC data do not include the portion of the ionosphere above the LEO altitude, whereas the GIM vertical TEC data do include it. The accuracy of the GIM vertical TEC data from the ionospherically quiet 4-day period analyzed in this paper should be quite good. The average difference between the GIM vertical TEC data and the TOPEX altimeter vertical TEC data (for an ionospherically quiet period in 1993) is close to 1 TECU [*Ho et al.*, 1997]. Thus the observed large mean differences are actually a statistically significant measure of supersatellite TEC (the amount of ionosphere above the LEO altitude of 735 km) during the 4-day period from February 20 to 23, 1997. An alternative method of computing supersatellite TEC is to use positive elevation angle measurements from a LEO, but this may be complicated by the estimation of L1/L2 interchannel biases. Supersatellite TEC information may be useful for studies of ionospheric climatology or possibly for ionospheric calibration of upcoming single-frequency altimeter missions.

Appendix A: Error Introduced by Unknown Refractivity at Low Earth Orbit Position

Refractivity can be reconstructed by means of an Abel inversion through calibrated bending angle or calibrated TEC data. When reconstructing a refractivity (electron density) profile through calibrated bending angles, the refractivity at the LEO position is used twice: when calculating the bending angle as a function of impact parameter from the Doppler frequency, and when inverting the calibrated bending angle (below the LEO) into the refractivity profile. When reconstructing a refractivity profile through calibrated TEC, the refractivity at the LEO position is not used at all. The assumption of straight-line propagation used in the TEC inversion is actually a linearization of the problem using the small parameter $\nu = 1 - n_{\mathrm{LEO}} << 1$. This means that when reconstructing refractivity from calibrated bending angle, the result also should not depend on the refractivity at the LEO position in the first order of magnitude with respect to ν. Below we will calculate the first-order term of the dependence of the retrieved refractivity on ν and show that it is zero.

To simplify these calculations, we will assume that the LEO is circular and that the GPS satellite is at rest infinitively far away in the LEO plane. In this case, (4)-(6) transform into

$$f_d = -f\frac{v_{\mathrm{LEO}}}{c} n_{\mathrm{LEO}} \sin\phi_{\mathrm{LEO}} \tag{A1}$$

$$a = r_{\mathrm{LEO}} n_{\mathrm{LEO}} \sin\phi_{\mathrm{LEO}} \tag{A2}$$

$$\alpha_{AB} = -\phi_{\mathrm{LEO}} + \theta_B \tag{A3}$$

$$\alpha_{AC} = \phi_{\mathrm{LEO}} + \theta_C - \pi \tag{A4}$$

It can be seen from (A1) and (A2) that the impact parameter calculated from Doppler, $a = -f_d c r_{\mathrm{LEO}} / f v_{\mathrm{LEO}}$, does not depend on refractivity at the LEO position at all, while the bending angle does depend on refractivity at the LEO position through ϕ_{LEO} as shown below:

$$\phi_{\mathrm{LEO}} = \arcsin\left(a / r_{\mathrm{LEO}} n_{\mathrm{LEO}}\right) \tag{A5}$$

Calculating $\tilde{\alpha}(a) = \alpha_{BC}(a) = \alpha_{AC}(a) - \alpha_{AB}(a)$, then expanding it using the small parameter ν, and keeping the linear term yields

$$\tilde{\alpha}(a) = \tilde{\alpha}_0(a) + \frac{2a\nu}{\sqrt{r_{\mathrm{LEO}}^2 - a^2}} + O(\nu^2) \tag{A6}$$

where $\tilde{\alpha}_0(a)$ is the bending angle calculated for $\nu = 0$. Substitution of (A6) into the inversion equation (equation (8)) gives

$$n(x) = (1-\nu)n_0(x)$$
$$\exp\left[\frac{\nu}{\pi}\int_x^{x_{LEO}} \frac{2ada}{\sqrt{(r_{LEO}^2 - a^2)(a^2 - x^2)}} + O(\nu^2)\right] \quad \text{(A7)}$$

where

$$n_0(x) = \exp\left[\frac{1}{\pi}\int_x^{x_{LEO}} \frac{\tilde{\alpha}_0(a)da}{\sqrt{a^2 - x^2}}\right] \quad \text{(A8)}$$

The upper limit of integration in (A7) may be changed from x_{LEO} to r_{LEO} by introducing an error of the second order of magnitude in ν, since $r_{LEO} - x_{LEO} = \nu r_{LEO}$. Then the integral may be calculated analytically, and the result is given by

$$n(x) = (1-\nu)n_0(x)\exp\left[\nu + O(\nu^2)\right]$$
$$= n_0(x) + O(\nu^2) \quad \text{(A9)}$$

Thus, for the inversion through calibrated bending angles, the refractivity at the LEO position may be set to 1 both when inverting Doppler into bending and when inverting bending into refractivity (electron density), by introducing an error of the second order of magnitude in $\nu = n_{LEO} - 1$, i.e., which is smaller than the first-order error estimated by *Hajj and Romans* [1998] for inversions through the uncalibrated bending angles.

Appendix B. Evaluation of the Impact of Orbit (LEO Velocity) Errors on Inversions

Here we evaluate the impact of the LEO velocity error (which is a dominant error source until precise orbit determination (POD) or dual-frequency inversions are used) on inversions through single-frequency bending angles and TECs. Equation (4) is written for the full Doppler frequency, f_d, which may be represented as a sum of vacuum Doppler, f_d^{vac} (due to the movement of satellites in vacuum), and excess Doppler, f_d^{exc} (the additional term related to the speeding up of phase and due to bending in the ionosphere). In practice, the first step of data processing is to calculate excess Doppler from the GPS/MET phase observables and the orbit data. Then (4), modified for the excess Doppler, is used to calculate bending angles. Thus in a strict sense the orbit data are used twice. However, the dominant error introduced by the LEO velocity errors appears at the first step, i.e., when calculating excess Doppler.

Again, as in Appendix A, we assume that the GPS satellite is at rest, infinitively far away in the circular LEO plane. In addition, we assume refractivity at the LEO position equal to 1. Then the equation (4) may be written in the form

$$f_d = f_d^{vac} + f_d^{exc} = -f\frac{v_{LEO}}{c}\sin\phi_{LEO} \quad \text{(B1)}$$

or

$$f_d^{exc} = f_d - f_d^{vac}$$
$$= -f\frac{v_{LEO}}{c}\left(\sin\phi_{LEO} - \sin\phi_{LEO}^{vac}\right)$$
$$\cong -f\frac{v_{LEO}}{c}\alpha\cos\phi_{LEO}^{vac} \quad \text{(B2)}$$

where α is a bending angle, and ϕ_{LEO} and ϕ_{LEO}^{vac} are the zenith angles at the LEO position of the true ray and of the straight-line ray, respectively.

To evaluate the magnitudes of f_d^{vac} and f_d^{exc} for mean ionospheric conditions, we take $f \cong 1.5$ GHz (L1 frequency), $v_{LEO} \cong 7$ km s^{-1}, $\alpha \cong 10^{-4}$ rad, $\cos\phi_{LEO}^{vac} \cong 0.4$, and $\sin\phi_{LEO}^{vac} \cong \sin\phi_{LEO} \cong 0.9$, and, which corresponds to about 200-km altitude, where the ionospheric effect is maximum, as seen in Figure 3. Then $f_d^{vac} = -fv_{LEO}\sin\phi_{LEO}^{vac}/c \cong 3\times10^4$ Hz, while $f_d^{exc} = -fv_{LEO}\alpha\cos\phi_{LEO}^{vac} \cong 1.5$ Hz.

When excess Doppler is calculated by differencing the calculated vacuum Doppler from the observed Doppler on the GPS-LEO link, then the LEO velocity error $\Delta v_{LEO} \cong 5$ cm s^{-1} (which is likely when POD is not applied) will transform into Doppler error $\Delta f_d = -f\Delta v_{LEO}\sin\phi_{LEO}^{vac}/c \cong 0.25$ Hz. This constitutes about 15% of the excess Doppler at the altitude of the maximal effect and hence is fractionally bigger at other altitudes and thus not negligible.

When calculating bending angle from the excess Doppler, as seen from (B2), the fractional LEO velocity error results in the same fractional bending angle error, $\Delta\alpha/\alpha \cong \Delta v_{LEO}/v_{LEO} \cong 10^{-5}$, and thus the impact of LEO velocity error at this step is negligible.

When performing inversions through TEC, the concept of bending angle is not used. However, the derivative of TEC, dT/dr_0, which is used in the inversion (see equation (14)), is directly related to excess Doppler, $dT/dr_0 \sim dS/dr_0 \sim f_d^{exc}/v_\perp$, where $v_\perp = v_{LEO}\cos\phi_{LEO}^{vac}$ is the tangent point descent rate, and hence its fractional error is the same as the fractional error of excess Doppler. Thus the impact of LEO velocity error on inversions through bending

angles and through TEC (in the assumption of straight-line propagation) is the same.

It is important that the error in excess phase, S, that is introduced by the LEO error, is a kinematic error, which does not depend on the frequency of radio waves, while the excess phase does depend on frequency due to dispersion of radio waves in the ionosphere. Thus the LEO velocity error (as well as GPS and LEO clock errors) is eliminated in dual-frequency inversions when TEC is calculated through $S_1 - S_2$ (see equation (11)), and in this case POD and the double-differencing technique are not required.

Acknowledgments. This work was supported by the Office of Naval Research (ONR) Space and Remote Sensing Program, grant number N00014-97-1-0712. The GPS/MET program was sponsored primarily by the National Science Foundation (NSF), with additional funding provided by the Federal Aviation Administration (FAA) and the National Oceanic and Atmospheric Administration (NOAA). In addition, the National Aeronautics and Space Administration (NASA) provided funding directly to the Jet Propulsion Laboratory (JPL) for support of GPS/MET. G. Ruffini and A. Flores at the Institut d'Estudis Espacials de Catalunya (IEEC) computed tomographic electron density fields used in this study. JPL provided the vertical TEC maps used in this study. The ionosonde data were provided by the National Geophysical Data Center (NGDC) in Boulder, Colorado. The authors are grateful to Randolph Ware (UCAR) for discussions and useful comments. The authors are also grateful to Dwight Decker and another anonymous referee for their many helpful comments that improved the paper.

References

Daniell, R. E., and L. D. Brown, PRISM: A parameterized real-time ionospheric specification model, Version 1.5, *Phillips Lab. Tech. Rep. PL-TR-95-2061*, 1995. (Available from Natl. Tech. Inf. Serv., Springfield, Va.)

Fjeldbo, G., A. J. Kliore, and V. L. Von Eshelman, The neutral atmosphere of Venus as studied with the Mariner V radio occultation experiments, *Astron. J., 76*, 123-140, 1971.

Flock, W. L., Propagation effects on satellite systems at frequencies below 10 GHz: A handbook for satellite systems design, 2nd ed., *NASA Ref. Publ. 1108*(02), 506 pp., 1987.

Hajj, G. A., and L. J. Romans, Ionospheric electron density profiles obtained with the Global Positioning System: Results from the GPS/MET experiment, *Radio Sci., 33*(1), 175-190, 1998.

Hajj, G. A., R. Ibanez-Meir, E. R. Kursinski, and L. J. Romans, Imaging the ionosphere with the Global Positioning System, *Int. J. Imaging Syst. Technol., 5*, 174-184, 1994.

Hardy, K. R., G. A. Hajj, E. R. Kursinski, and R. Ibanez-Meier, Accuracies of atmospheric profiles obtained from GPS occultations, in *Proceedings of the ION GPS-93 Conference*, pp. 1545-1556, Inst. of Navig., Alexandria, Va., 1993.

Ho, C. M., B. D. Wilson, A. J. Mannucci, U. J. Lindqwister, and D. N. Yuan, A comparative study of ionospheric total electron content measurements using global ionospheric maps of GPS, TOPEX radar, and the Bent model, *Radio Sci., 32*(4), 1499-1512, 1997.

Howe, B. M., K. Runciman, and J. A. Secan, Tomography of the ionosphere: Four-dimensional simulations, *Radio Sci., 33*(1), 109-128, 1998.

Kursinski, R., et al., Initial results of radio occultation observations of Earth's atmosphere using the Global Positioning System, *Science, 271*, 1107-1110, 1996.

Leitinger, R., H.-P. Ladreiter, and G. Kirchengast, Ionosphere tomography with data from satellite reception of Global Navigation Satellite System signals and ground reception of Navy Navigation Satellite System signals, *Radio Sci., 32*(4), 1657-1669, 1997.

Mannucci, A. J., B. D. Wilson, D. N. Yuan, C. H. Ho, U. J. Lindqwister, and T. F. Runge, A global mapping technique for GPS-derived ionospheric total electron content measurements, *Radio Sci., 33*(3), 565-582, 1998.

Phinney, R. A., and D. L. Anderson, On the radio occultation method for studying planetary atmospheres, *J. Geophys. Res., 73*(5), 1819-1827, 1968.

Rius, A., G. Ruffini, and L. Cucurull, Improving the vertical resolution of ionospheric tomography with GPS occultations, *Geophys. Res. Lett., 24*(18), 2291-2294, 1997.

Rocken, C., R. et al., Analysis and validation of GPS/MET data in the neutral atmosphere, *J. Geophys. Res, 102*(D25), 29,849-29,866, 1997.

Schreiner, W. S., D. C. Hunt, C. Rocken, and S. V. Sokolovskiy, Precise GPS data processing for the GPS/MET radio occultation mission at UCAR, in *Proceedings of the Institute of Navigation - Navigation 2000*, pp. 103-112, Alexandria, Va., 1998.

Ware, R., et al., GPS sounding of the atmosphere from low Earth orbit: Preliminary results, *Bull. Am. Meteorol. Soc., 77*, 19-40, 1996.

D.C. Hunt, C. Rocken, W. S. Schreiner, and S. V. Sokolovskiy, University Corporation for Atmospheric Research, 3300 Mitchell Lane, Suite 390, PO Box 3000, Boulder, CO 80301. (dhunt @ucar.edu; rocken@ucar.edu; schrein@ucar.edu; sergey @ucar.edu)

(Received September 23, 1998; revised March 10, 1999; accepted March 12, 1999.)